Detecting Magnetoelectric Effect in a Metallic Antiferromagnet via Nonreciprocal Rotation of Reflected Light

Keito Arakawa,[1,*] Takeshi Hayashida,[1,*] Kenta Kimura,[1,2] Ryusuke Misawa,[1] Takayuki Nagai,[1,3] Tatsuya Miyamoto,[1] Hiroshi Okamoto,[1] Fumitoshi Iga,[4] and Tsuyoshi Kimura[1,5,†]

[1]*Department of Advanced Materials Science, University of Tokyo, Kashiwa, Chiba 277-8561, Japan*
[2]*Department of Materials Science, Osaka Metropolitan University, Sakai, Osaka 599-8531, Japan*
[3]*Quantum-Phase Electronics Center (QPEC) and Department of Applied Physics, University of Tokyo, Bunkyo-ku, Tokyo 113-8656, Japan*
[4]*Institute of Quantum Beam Science, Ibaraki University, Mito, Ibaraki 310-8512, Japan*
[5]*Department of Applied Physics, University of Tokyo, Bunkyo-ku, Tokyo 113-8656, Japan*

(Received 30 June 2023; accepted 2 November 2023; published 5 December 2023)

Certain types of media breaking both space-inversion (P) and time-reversal (T) symmetries but preserving their combination PT exhibit the polarization rotation of reflected light even when that of transmitted light is prohibited. Such an effect is termed nonreciprocal rotation of reflected light (NRR). Although NRR shows nearly the same phenomenon as the magnetooptical Kerr effect or, equivalently, the Hall effect at optical frequencies, its origin is distinct and ascribed to a magnetoelectric (ME) effect at optical frequencies, i.e., the optical ME effect. Here we show the observation of NRR in a metallic antiferromagnet TbB_4. The result demonstrates that the ME effect in a metallic system, which is considered to be ill defined, can be detected using reflected light. Furthermore, we spatially resolve antiferromagnetic domains in TbB_4 by microscope observations of NRR. Our work offers a unique way to probe the ME effect in metallic systems.

DOI: 10.1103/PhysRevLett.131.236702

Recently, antiferromagnetic (AFM) materials have attracted growing interest from the perspective of spintronics technologies [1–3]. However, detection and control of the AFM states are nontrivial due to compensated magnetization. One of the promising ways to overcome the difficulties is to utilize properties caused by breaking both space-inversion (P) and time-reversal (T) symmetries but preserving the combined PT symmetry. Such a symmetry state occurs in particular AFM materials and induces unique couplings between electric and magnetic properties. One of the well-known couplings is the linear magnetoelectric (ME) effect; that is, the induction of electric polarization P (magnetization M) by an applied magnetic field H (electric field E) [4–7]. Though the ME effect has long been studied in various magnetic materials, most of the former experimental studies have targeted insulating materials. This is mainly because the ME effect is ill defined in metallic materials where free electrons screen an applied electric field and polarization. Instead, an electric current can interact with magnetization in metallic systems [8]. In metallic ferromagnets with broken P symmetry, current-induced switching of magnetization due to the spin torque has been reported [9,10]. In a similar manner, current-induced switching of AFM domain states has been observed in metallic antiferromagnets in which spin orderings break both P and T symmetries but preserve the combined PT symmetry [11,12]. Notably, the similarity between the ME effect in insulators and the current-induced switching of magnetic properties in metals has been discussed based on the theory of cluster multipoles and the linear-response theory [13,14].

The linear ME effect responding to a static field is not well defined in metallic materials, but that is not the case when the effect is expanded to optical frequencies. That is called the optical magnetoelectric (OME) effect in which $P(\omega)[M(\omega)]$ is induced by oscillating $H(\omega)[E(\omega)]$ of an electromagnetic wave with an angular frequency ω and expressed as $P_i(\omega) = \alpha_{ij}(\omega)H_j(\omega)$ $[\mu_0 M_i(\omega) = \alpha_{ji}(\omega)E_j(\omega)]$. Here $\alpha_{ij}(\omega)$ is the ME tensor of the OME effect, i and j run over all the Cartesian coordinates, and μ_0 is the permeability of vacuum. The OME effect induces nonreciprocal optical phenomena [15] including nonreciprocal directional dichroism (NDD), that is, asymmetry in absorption between counterpropagating light beams. NDD originates from the off-diagonal components of $\alpha_{ij}(\omega)$ and has been observed in various systems breaking P and T symmetries [16–19]. At optical frequencies where the screening of electric fields is no longer effective, $P(\omega)$ or $E(\omega)$ can be defined even in metals, and thus the OME effect should be observed regardless of the sample conductivity. This suggests that ME couplings in metallic systems can be detected at optical frequencies. However, the OME effect in metallic systems has been little studied experimentally.

For the observation of OME effects in metals, an effect of reflected light, nonreciprocal rotation of reflected light (NRR) [20–22], is suitable. NRR refers to the rotation of the polarization plane of reflected light, which is similar to the well-known magneto-optical Kerr effect (MOKE). However, these two effects are distinct from each other from the perspective of symmetry breakings [23]. MOKE requires breaking of T and PT symmetries, and thus it has been used for probing the signature of T-symmetry breaking in various exotic quantum materials [24]. Furthermore, its microscopic origin is related to the Hall effect at optical frequencies [23,25]. On the other hand, NRR is ascribed to the ME effect and requires breaking of both T and P symmetries [20–22,26,27]. More particularly, NRR is allowed in materials that have finite diagonal components of the ME tensor $\alpha_{jj}(\omega)$ [27]. So far, NRR has been observed in the archetypical ME antiferromagnet Cr_2O_3 with finite $\alpha_{jj}(\omega)$ [21,22]. Recently AFM domains of Cr_2O_3 have been visualized using NRR [28,29]. We consider that NRR will provide not only a unique way to elucidate the ME effect in metallic antiferromagnets but also a new probe to read out their AFM states. In this study, we demonstrate the optical detection of an ME effect in a metallic antiferromagnet with broken P and T symmetries but preserved PT symmetry and reveal its AFM domain states via NRR.

As a target metallic ME antiferromagnet to observe NRR, we chose TbB_4, one of the rare-earth tetraborides RB_4 (R = rare-earth elements) with the $P4/mbm$ tetragonal structure [Fig. 1(a)]. They have attracted interest from the viewpoints of geometrical frustration and orbital order [30–35]. In addition, some of the tetraborides have been discussed as systems showing a linear ME effect because their AFM structures break both P and T symmetries but preserve the combined PT symmetry [36–38]. However, their linear ME effect has never been observed because of their metallic nature. Figure 1(b) shows the temperature profiles of resistivity and M/H of our TbB_4 crystal. TbB_4 shows very low resistivity (10^{-7} Ω cm at 2 K) [39] and undergoes two successive magnetic phase transitions at $T_{N1} = 44$ and $T_{N2} = 24$ K [30]. No spontaneous M is observed in all the phases, indicating that M is fully compensated. The magnetic structure at $T_{N2} \leq T \leq T_{N1}$ (AFM1 phase) [Fig. 1(a)] is characterized by the noncollinear spin configuration in which Tb moments are aligned in the ⟨110⟩ directions [31]. The magnetic point group of the AFM1 phase is $4/m'm'm'$ in which diagonal terms of the ME tensor are finite [$\alpha_{11}, \alpha_{22}(=\alpha_{11})$, and α_{33}] [40] and therefore allows NRR [27]. There are two distinct domain states (A+ and A−) related to each other by either T ($1'$) or P ($\bar{1}$) operations [Fig. 1(a)].

We apply the symmetry-based discussion of NRR [20–22] to TbB_4. When linearly polarized incident light is irradiated along the c axis in the AFM1 phase, the polarization plane of reflected light could rotate due to NRR ascribed to finite

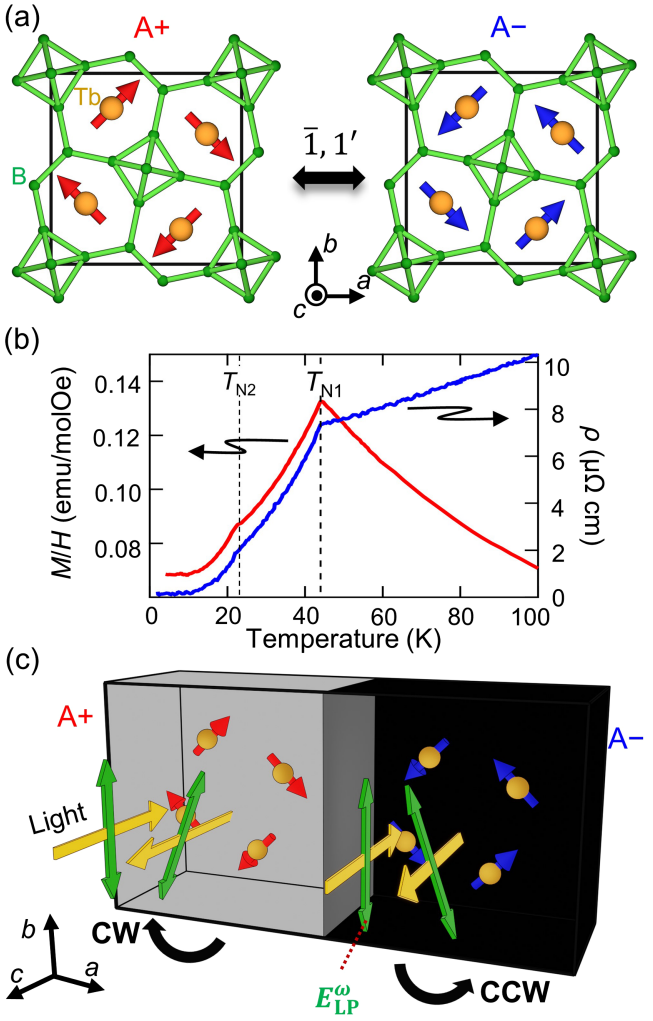

FIG. 1. (a) Crystal and magnetic structures in the AFM1 phase [$T_{N2} \leq T \leq T_{N1}$] of TbB_4. Red and blue arrows denote Tb moments. Two distinct domain states (A+ and A−) related by either space-inversion operation ($\bar{1}$) or time-reversal operation ($1'$) are depicted. (b) Temperature profiles of M/H along the a axis and resistivity normal to the c axis. (c) A schematic image of nonreciprocal rotation of reflected light (NRR). The polarization plane (green arrows) of light reflected from the ab face of TbB_4 is rotated in opposite directions for the two distinct domains.

$\alpha_{jj}(\omega)$. The rotation angle θ and the ellipticity η are described as [20–22]

$$\theta + i\eta = \frac{2\alpha_{\perp}(\omega)\left[1 + N_{\perp}(\omega)\right]}{1 - N_{\perp}(\omega)}. \quad (1)$$

Here, $\alpha_{\perp}(\omega) = [\alpha_{11}(\omega) + \alpha_{22}(\omega)]/2$ is the in-plane ME coefficient expanded to the optical frequencies ω and $N_{\perp}(\omega)^2 = [\epsilon_{11}(\omega) + \epsilon_{22}(\omega)]/2$ corresponds to the in-plane dielectric constant. Though Eq. (1) was derived to explain NRR in insulators [20,22], it can be applied to that in metals by treating both $\alpha_{\perp}(\omega)$ and $N_{\perp}(\omega)$ as complex numbers. The signs of the ME tensor are opposite between the two domain

states, and thus the directions of NRR, i.e., the signs of θ (and η) are also opposite between the two. Therefore, AFM domains in TbB_4 can be visualized by spatial distribution measurements of NRR [Fig. 1(c)].

The magnitude of NRR reported in previous studies is relatively small ($10^{-5} \sim 10^{-4}$ rad for θ and η in Cr_2O_3) [22,28]. To obtain two-dimensional maps of such a small effect, we adopted a difference image sensing technique using polarization modulation of incident light [28,41]. Details of the technique are described in the Supplemental Material [42]. In this technique, θ and η are spatially resolved from a difference between reflection microscope images obtained by using differently polarized incident light. When θ and η are small and η is small enough compared with θ, a normalized difference between the intensities of reflected light under linearly polarized light (I_{LP}) and right circularly polarized light (I_{RCP}) irradiation is written as $\Delta I/I \equiv (I_{\mathrm{LP}} - I_{\mathrm{RCP}})/2I_{\mathrm{RCP}} \approx \theta$ [Supplemental Material Eq. (S1) [42]]. When $|\eta|$ is comparable with $|\theta|$, the η component also contributes to $\Delta I/I$ signals. In any case, spatially resolved measurements of $\Delta I/I$ reveal spatial distributions of NRR, which correspond to ME (or AFM) domains.

Figures 2(a)–2(c) show two-dimensional maps of $\Delta I/I$ in the paramagnetic and AFM1 phases. Here, the direction of light propagation is along the c axis, and the photon energy of incident light is 2.10 eV. The polarization direction of linearly polarized incident light (E^{ω}_{LP}) was set along $[1\bar{1}0]$ [inset of Fig. 2(a)]. In the paramagnetic phase (50 K), $\Delta I/I$ signals are weak and uniform [Fig. 2(a)], meaning that NRR is zero over the entire sample. By contrast, in the AFM1 phase (35 K), clear light and dark contrasts, between which the sign of NRR is opposite, are observed [Figs. 2(b) and 2(c)]. The cooling sequence was repeated twice with heating up to room temperature in between, and the results obtained in the first and second sequences are shown in Fig. 2(b) and Fig. 2(c), respectively. The contrast patterns obtained in the first and second cooling sequences are different from each other, which suggests that such domains were formed by undergoing the transition into the AFM1 phase. The typical domain size ranged from several tens to several hundreds of micrometers.

To investigate the temperature dependence of NRR signals, we obtained $\Delta I/I$ maps at various temperatures. As seen in the insets of Fig. 2(d), no contrast is observed in the $\Delta I/I$ map at temperatures above T_{N1} while the contrast gets stronger with decreasing temperature below T_{N1}. To evaluate the magnitude of NRR, we obtained a difference in $\Delta I/I$ at A+ and A− domains, $|(\Delta I/I)_{\mathrm{A}+} - (\Delta I/I)_{\mathrm{A}-}|$, by averaging the results of 10 pairs of nearby opposite domains. Also, to remove backgrounds, $|(\Delta I/I)_{\mathrm{A}+} - (\Delta I/I)_{\mathrm{A}-}|$ at 60 K ($>T_{\mathrm{N1}}$) was subtracted from that at each temperature. Figure 2(d) shows the obtained temperature dependence of $|(\Delta I/I)_{\mathrm{A}+} - (\Delta I/I)_{\mathrm{A}-}|$ which develops below T_{N1} and

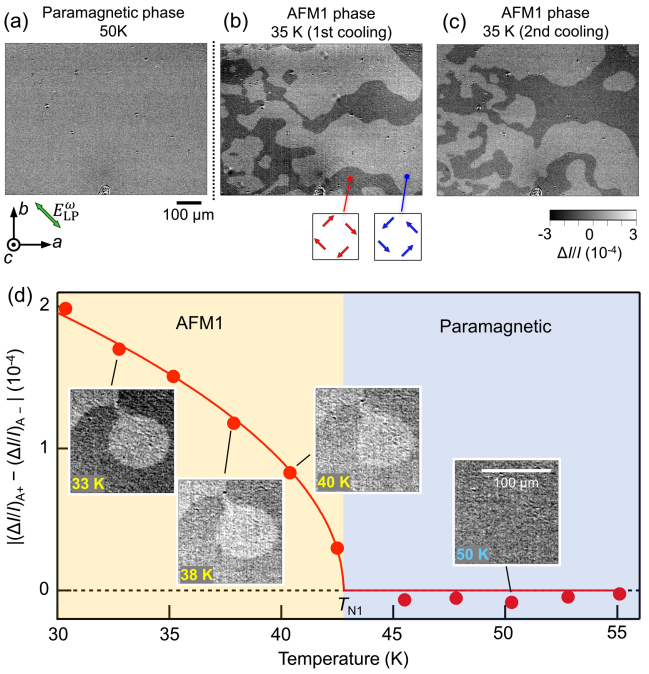

FIG. 2. Spatial distributions of NRR in TbB_4. (a)–(c) Two-dimensional maps of $\Delta I/I$, which approximately correspond to the polarization rotation of reflected light, at 50 (a) and 35 K (b), (c). These maps were obtained in the same area of the specimen. The map of (b) was obtained during the first cooling. Then, that of (c) was obtained during the second cooling after the sample was heated above T_{N1}. Schematic illustrations in (b) depict the expected domain states in the respective contrast regions. (d) Temperature dependence of the difference between $\Delta I/I$ at the light and dark areas, i.e., A+ and A− domains, $|(\Delta I/I)_{\mathrm{A}+} - (\Delta I/I)_{\mathrm{A}-}|$, which is proportional to the magnitude of NRR. The insets of (d) display $\Delta I/I$ maps used to obtain the difference at the respective temperatures. The red curve is a guide to the eye.

increases with decreasing temperature. The temperature evolution agrees well with that of the magnetic order parameter obtained by resonant x-ray diffraction [46], indicating that NRR is effective to detect magnetic order in ME antiferromagnets with the diagonal ME effect.

Below T_{N2} (AFM2 phase), Tb moments tilt toward the a or b axis from $\langle 110 \rangle$, which breaks the four-fold rotational symmetry. This transition accompanies a structural phase transition from tetragonal to orthorhombic [34,46], and the magnetic point group in the AFM2 phase is reduced to $m'm'm'$. As illustrated in Supplemental Material Fig. S2 [42], the AFM2 phase holds four domain states: the pairs related by either $1'$ or $\bar{1}$ and the pairs related by the fourfold rotational operation (4). This magnetic symmetry also holds a finite diagonal ME tensor (α_{11}, α_{22}, and α_{33}) and allows NRR [27]. However, in addition to NRR, linear birefringence will be introduced by the four-fold rotational symmetry breaking. Thus, the polarization rotation of reflected light is caused not only via NRR but also the linear birefringence.

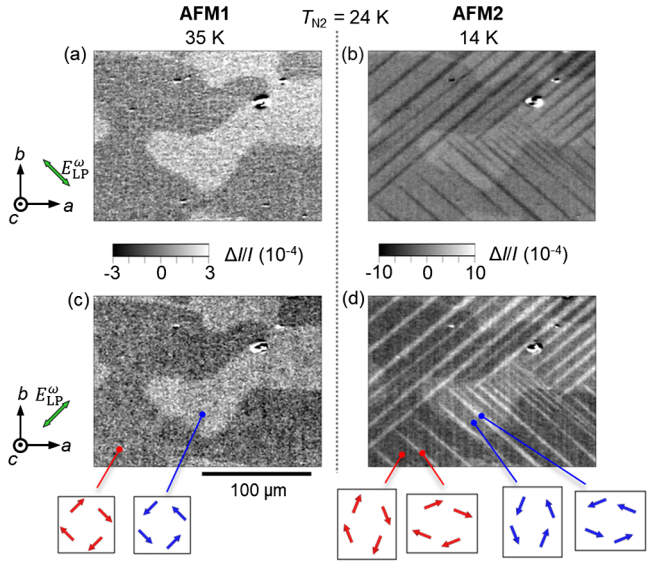

FIG. 3. Antiferromagnetic domains in the two AFM phases. $\Delta I/I$ maps at 35 K in the AFM1 phase (a),(c) and at 14 K in the AFM2 phase (b),(d). The incident linearly polarization light (E^{ω}_{LP}) was set along $[1\bar{1}0]$ for (a),(b) and along [110] for (c),(d). Schematic illustrations depict the expected domain states in the respective contrast regions.

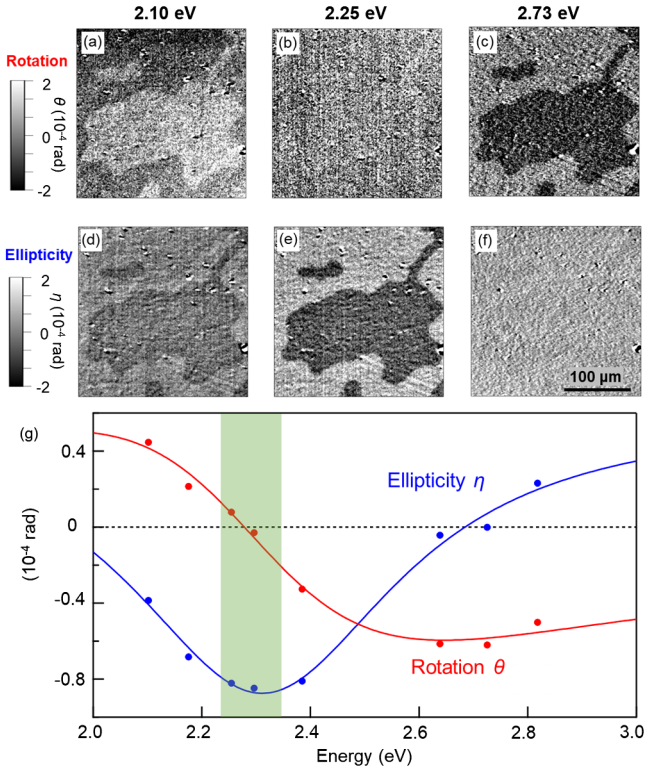

FIG. 4. NRR spectra in the AFM1 phase. (a)–(f) Two-dimensional maps of the rotation angle θ (a)–(c) and the ellipticity η (d)–(f) at 34 K with monochromatic light whose photon energy is 2.10 (left), 2.25 (middle), and 2.73 eV (right). (g) Spectra of θ and η. θ crosses the zero line at approximately 2.3 eV (green-colored area) while η shows a peak. The red and blue curves are guides to the eye.

Figures 3(a) and 3(b) display $\Delta I/I$ maps at the same area in the AFM1 and AFM2 phases, respectively. In the AFM2 phase [Fig. 3(b)], stripe patterns are superimposed on the domain patterns observed in the AFM1 phase [Fig. 3(a)]. The stripes are along [110] or $[1\bar{1}0]$. To elucidate the origins of the polarization rotation of reflected light in the AFM1 and AFM2 phases, we measured $\Delta I/I$ maps with changing the direction of the polarization of incident light. The domain contrasts of the AFM1 phase remain unchanged between the two different polarization settings of $E^{\omega}_{LP}//[1\bar{1}0]$ and [110] [compare Fig. 3(a) and Fig. 3(c)]. This result indicates that the polarization rotation of reflected light in the AFM1 phase comes from NRR which is independent of the incident light polarization direction. By contrast, the contrasts of the stripe patterns in the AFM2 phase get reversed between the two different polarization settings [compare Figs. 3(b) and 3(d)]. This result indicates that the stripe patterns in the AFM2 phase are due to the linear birefringence caused by the tetragonal-orthorhombic structural distortion. Note that the rounded domain patterns in the AFM2 phase, which already exist in the AFM1 phase, do not show contrast reversal. The schematic illustrations in Fig. 3 depict the expected domain states in the respective contrast regions. Thus, we can spatially resolve the four domain states using the polarization rotation of reflected light.

To discuss the microscopic origin of NRR in TbB_4, we performed the domain observation measurements at several photon energies in the AFM1 phase. To evaluate θ and η ascribed to NRR accurately, we took a normalized difference between the intensities of reflected light under right and left circularly polarized light irradiation. The difference is written as $\Delta\tilde{I}/\tilde{I} \equiv (I_{RCP} - I_{LCP})/[2(I_{RCP} + I_{LCP})] \approx \eta$ [Supplemental Material Eq. (S2)]. Figures 4(d), 4(e), and 4(f) show the $\Delta\tilde{I}/\tilde{I}$ (or η) maps obtained at 2.10, 2.25, and 2.73 eV, respectively, at 34 K. The domain contrast in the η maps is the most pronounced at 2.25 eV. The θ components in the $\Delta I/I$ maps are extracted by calculations using the $\Delta\tilde{I}/\tilde{I}$ maps. Figures 4(a)–4(c) show the obtained θ maps. The domain contrast in the θ maps is reversed between the images obtained at 2.10 [Fig. 4(a)] and 2.73 eV [Fig. 4(c)], and no contrast is observed at 2.25 eV [Fig. 4(b)]. This result indicates that the sign of θ is reversed around 2.25 eV. We evaluated the magnitude of θ and η at the respective energies in the same way as the data analysis used for Fig. 2(d). Figure 4(g) shows the obtained θ and η spectra. The θ spectrum crosses the zero line at 2.3 eV, and the η spectrum takes a peak at the same energy, which is consistent with the Kramers-Kronig relation between θ and η. These spectral features suggest that a characteristic electronic transition contributing to NRR is located at around 2.3 eV.

A possible origin is the f-f transitions of electrons localized on Tb^{3+} ions. Microscopically, the interference of electric dipole ($E1$) and magnetic dipole ($M1$) transitions mediated by the spin-orbit interaction contributes to NRR. The contribution to $\alpha_{jj}(\omega)$ from a single Tb^{3+} ion can be described as [22,47]

$$\alpha_{jj}(\omega) \propto \sum_{k,n} \rho_k \left\{ \frac{\mathrm{Re}[\langle k|M_j|n\rangle\langle n|P_j|k\rangle]}{\omega_{nk} - \omega - i\Gamma_{nk}} + \frac{\mathrm{Re}[\langle k|P_j|n\rangle\langle n|M_j|k\rangle]}{\omega_{nk} + \omega + i\Gamma_{nk}} \right\}, \quad (2)$$

where k and n are single-ion states, ρ_k is an occupation probability of the state k, $\hbar\omega_{nk}$ is an energy difference between those eigenstates, Γ_{nk} is a damping factor, P_j (M_j) is an electric (magnetic) dipole moment. In Eq. (2), the real part of $\alpha_{jj}(\omega)$ shows a dispersive structure, i.e., a sign reversal, around the resonance frequency ω_{nk}, while the imaginary part of $\alpha_{jj}(\omega)$ shows an absorptive structure, i.e., a single peak structure around ω_{nk}.

The ground state of the localized $4f$ ions on Tb^{3+} is $^7F_6$. The lowest excitations have been assigned to the transition from $^7F_6$ to $^5D_4$, whose excitation energy is about 2.5 eV [48,49]. This excitation energy is slightly away from the energy at which the characteristic behavior of NRR was observed. However, it is possible that the mixing between the Tb $4f$ state with the boron $2s$ and $2p$ states changes the excitation energy. Thus, the f-f transition from $^7F_6$ to $^5D_4$ can contribute to NRR in TbB_4. Although both $E1$ and $M1$ transitions are originally forbidden between $^7F_6$ and $^5D_4$, they will be allowed with the aid of the noncentrosymmetric crystal field around the Tb^{3+} site (site symmetry C_{2v}) and the mixing of the different total angular momentum J (J-mixing) due to the crystal field [50,51]. We note that the refractive index $N(\omega)$ can also influence the NRR spectrum [see Eq. (1)]. Supplemental Material Fig. S3 shows the real (n) and imaginary (κ) parts of $N(\omega)$, which were calculated from the reflection spectrum by using the Kramers-Kronig transformation [42]. They are almost flat in the range of 2.0 to 3.0 eV, meaning that $N(\omega)$ has less effect on the structure of the NRR spectrum. By contrast, an overall feature of the NRR spectrum resembles the energy profile of $\alpha_\perp(\omega)$ calculated from the experimental data of θ, η, n, and κ based on Eq. (1) (see Supplemental Material Fig. S4 [42]). Thus, the energy profile of NRR shown in Fig. 4(g) largely reflects that of $\alpha_\perp(\omega)$.

Finally, we briefly compare the NRR technique with existing techniques as a tool for the AFM domain imaging of metallic systems. Note that there are several types of AFM domains such as configuration, orientation, 180°, and chirality domains [52]. The observation technique depends on the domain type. The AFM domain revealed in this NRR study belongs to the 180° domain where a pair of domains are converted into each other by the time-reversal operation. However, the imaging techniques for the 180° AFM domain in metallic systems are limited. Examples of such techniques include spin-polarized scanning tunneling microscopy [52,53] and differential phase contrast imaging in scanning transmission electron microscopy [54]. These two techniques allow for domain imaging on an atomic scale without the need for specific symmetry breakings. However, their domain observation area is restricted to nanometer scales, and it is hard to carry out *in situ* measurements of macroscopic properties such as transport properties. In contrast, domain imaging using NRR offers broad-area observation up to millimeter scales, advantageous for monitoring domain responses to external fields (e.g., electrical current) and for verifying the correlation between the domain state and macroscopic properties. While second harmonic generation (SHG) is another plausible technique [52,55] and shares similar benefits with the NRR technique, it has never been applied to metallic AFM systems.

In conclusion, we succeeded in observing an optical magnetoelectric (OME) effect, nonreciprocal rotation of reflected light (NRR), in the metallic antiferromagnet TbB_4. Spatial distribution measurements of polarization rotation angle visualized AFM domain structures of TbB_4. In contrast to AFM domains in ME insulators, which can be controlled by the simultaneous application of magnetic and electric fields, it is still difficult to control AFM domains in ME metals. Recently, switching of AFM domain states using an inverse effect of NRR was reported in a topological axion insulator $MnBi_2Te_4$ [56]. Such an inverse effect of NRR will also be effective to control AFM domains of ME metals. Our achievements provide a new probe for the spatially resolved detection of symmetry breakings in metallic compounds.

We thank Y. Tanaka for fruitful discussions. This work was supported by the World-Leading Innovative Graduate Study Program for Materials Research, Industry, and Technology (MERIT-WINGS) of the University of Tokyo, the MEXT Leading Initiative for Excellent Young Researchers (LEADER), and by JSPS KAKENHI Grants No. JP19H05823, No. JP19H01847, No. JP21H04436, No. JP21H04988, and No. JP22J11247.

*These authors contributed equally to this work.
†Corresponding author: tkimura@ap.t.u-tokyo.ac.jp

[1] T. Jungwirth, X. Marti, P. Wadley, and J. Wunderlich, Nat. Nanotechnol. **11**, 231 (2016).
[2] V. Baltz, A. Manchon, M. Tsoi, T. Moriyama, T. Ono, and Y. Tserkovnyak, Rev. Mod. Phys. **90**, 015005 (2018).
[3] P. Němec, M. Fiebig, T. Kampfrath, and A. V. Kimel, Nat. Phys. **14**, 229 (2018).
[4] I. E. Dzyaloshinskii, Zh. Exp. Teor. Fiz. **33**, 881 (1959).
[5] D. N. Astrov, Zh. Exp. Teor. Fiz. **38**, 984 (1960).

[6] H. Schmid, Magnetoelectric effects in insulating magnetic materials, in *Introduction to Complex Mediums for Optics and Electromagnetics*, edited by W. S. Weiglhofer and A. Lakhtakia (SPIE Press, Bellingham, 2003), 167.

[7] M. Fiebig, J. Phys. D **38**, R123 (2005).

[8] A. Manchon, J. Železný, I. M. Miron, T. Jungwirth, J. Sinova, A. Thiaville, K. Garello, and P. Gambardella, Rev. Mod. Phys. **91**, 035004 (2019).

[9] A. Chernyshov, M. Overby, X. Liu, J. K. Furdyna, Y. Lyanda-Geller, and L. P. Rokhinson, Nat. Phys. **5**, 656 (2009).

[10] I. M. Miron, G. Gaudin, S. Auffret, B. Rodmacq, A. Schuhl, S. Pizzini, J. Vogel, and P. Gambardella, Nat. Mater. **9**, 230 (2010).

[11] P. Wadley *et al.*, Science **351**, 587 (2016).

[12] M. J. Grzybowski, P. Wadley, K. W. Edmonds, R. Beardsley, V. Hills, R. P. Campion, B. L. Gallagher, J. S. Chauhan, V. Novak, T. Jungwirth, F. Maccherozzi, and S. S. Dhesi, Phys. Rev. Lett. **118**, 057701 (2017).

[13] H. Watanabe and Y. Yanase, Phys. Rev. B **98**, 220412(R) (2018).

[14] F. Thöle, A. Keliri, and N. A. Spaldin, J. Appl. Phys. **127**, 213905 (2020).

[15] Y. Tokura and N. Nagaosa, Nat. Commun. **9**, 3740 (2018).

[16] G. L. J. A. Rikken, C. Strohm, and P. Wyder, Phys. Rev. Lett. **89**, 133005 (2002).

[17] M. Saito, K. Taniguchi, and T. H. Arima, J. Phys. Soc. Jpn. **77**, 013705 (2008).

[18] K. Kimura, T. Katsuyoshi, Y. Sawada, S. Kimura, and T. Kimura, Commun. Mater. **1**, 39 (2020).

[19] K. Kimura, Y. Otake, and T. Kimura, Nat. Commun. **13**, 697 (2022).

[20] R. M. Hornreich and S. Shtrikman, Phys. Rev. **171**, 1065 (1968).

[21] B. B. Krichevtsov, V. V. Pavlov, R. V. Pisarev, and V. N. Gridnev, J. Phys. Condens. Matter **5**, 8233 (1993).

[22] B. B. Krichevtsov, V. V. Pavlov, R. V. Pisarev, and V. N. Gridnev, Phys. Rev. Lett. **76**, 4628 (1996).

[23] J. Ahn, S. Y. Xu, and A. Vishwanath, Nat. Commun. **13**, 7615 (2022).

[24] A. Kapitulnik, J. Xia, E. Schemm, and A. Palevski, New J. Phys. **11**, 055060 (2009).

[25] W. Feng, G. Y. Guo, J. Zhou, Y. Yao, and Q. Niu, Phys. Rev. B **92**, 144426 (2015).

[26] J. Orenstein, Phys. Rev. Lett. **107**, 067002 (2011).

[27] E. B. Graham and R. E. Raab, Phys. Rev. B **59**, 7058–7063 (1999).

[28] T. Hayashida, K. Arakawa, T. Oshima, K. Kimura, and T. Kimura, Phys. Rev. Res. **4**, 043063 (2022).

[29] X. D. Zhu, J. Magn. Magn. Mater. **570**, 170371 (2023).

[30] Z. Fisk, M. B. Maple, D. C. Johnston, and L. D. Woolf, Solid State Commun. **39**, 1189 (1981).

[31] T. Matsumura, D. Okuyama, and Y. Murakami, J. Phys. Soc. Jpn. **76**, 015001 (2007).

[32] S. Yoshii, T. Yamamoto, M. Hagiwara, S. Michimura, A. Shigekawa, F. Iga, T. Takabatake, and K. Kindo, Phys. Rev. Lett. **101**, 087202 (2008).

[33] K. Siemensmeyer, E. Wulf, H.-J. Mikeska, K. Flachbart, S. Gabáni, S. Mat'aš, P. Priputen, A. Efdokimova, and N. Shitsevalova, Phys. Rev. Lett. **101**, 177201 (2008).

[34] V. V. Novikov, N. V. Mitroshenkov, A. V. Morozov, A. V. Matovnikov, and D. V. Avdashchenko, J. Therm. Anal. Calorim. **113**, 779 (2013).

[35] H. Sim, S. Lee, K.-P. Hong, J. Jeong, J. R. Zhang, T. Kamiyama, D. T. Adroja, C. A. Murray, S. P. Thompson, F. Iga, S. Ji, D. Khomskii, and J.-G. Park, Phys. Rev. B **94**, 195128 (2016).

[36] S. W. Lovesey, J. Fernández Rodríguez, J. A. Blanco, and P. J. Brown, Phys. Rev. B **70**, 172414 (2004).

[37] S. W. Lovesey, E. Balcar, K. S. Knight, and J. Fernández Rodríguez, Phys. Rep. **411**, 233 (2005).

[38] H. Watanabe and Y. Yanase, Phys. Rev. B **98**, 245129 (2018).

[39] J. S. Rhyee, J. Y. Kim, and B. K. Cho, J. Appl. Phys. **101**, 09D509 (2007).

[40] R. R. Birss, *Symmetry & Magnetism* (North-Holland Publishing Company, Amsterdam, 1966).

[41] T. Ishibashi, Z. Kuang, S. Yufune, T. Kawata, M. Oda, T. Tani, Y. Iimura, K. Sato, Y. Konishi, K. Akahane, X. Zhao, and T. Hasegawa, J. Appl. Phys. **100**, 093903 (2006).

[42] See Supplemental Material at http://link.aps.org/supplemental/10.1103/PhysRevLett.131.236702 for details of the experimental methods, the NRR microscope system, two antiferromagnetic phases and their domain states in TbB_4, the reflectance spectrum of TbB_4, and the energy profile of the ME coefficient in TbB_4. Supplemental Material includes Refs. [28,41,43–45].

[43] F. Iga, N. Shimizu, and T. Takabatake, J. Magn. Magn. Matter. **177**, 337 (1998).

[44] T. K. Fujita, M. Yoshizawa, R. Kamiya, H. Mitamura, T. Sakakibara, K. Kindo, F. Iga, I. Ishii, and T. Suzuki, J. Phys. Soc. Jpn. **80**, SA084 (2011).

[45] K. Momma and F. Izumi, J. Appl. Crystallogr. **44**, 1272 (2011).

[46] H. Huang, H. Jang, B. Y. Kang, B. K. Cho, C.-C. Kao, Y.-J. Liu, and J.-S. Lee, Curr. Appl. Phys. **18**, 1205 (2018).

[47] M. Muto, Y. Tanabe, T. Iizuka-Sakano, and E. Hanamura, Phys. Rev. B **57**, 9586 (1998).

[48] R. W. Schwartz, H. G. Brittain, J. P. Riehl, W. Yeakel, and F. S. Richardson, Mol. Phys. **34**, 361 (1977).

[49] K. Taniguchi, M. Nishio, S. Kishiue, P.-J. Huang, S. Kimura, and H. Miyasaka, Phys. Rev. Mater. **3**, 045202 (2019).

[50] M. Tanaka, G. Nishimura, and T. Kushida, Phys. Rev. B **49**, 16917 (1994).

[51] Y. Shimada, H. Kiyama, and Y. Tokura, Phys. Rev. B **75**, 245125 (2007).

[52] S.-W. Cheong, M. Fiebig, W. Wu, L. Chapon, and V. Kiryukhin, npj Quantum Mater. **5**, 3 (2020).

[53] M. Bode, E. Y. Vedmedenko, K. von Bergmann, A. Kubetzka, P. Feerriani, S. Heinze, and R. Wiesendanger, Nat. Mater. **5**, 477 (2006).

[54] Y. Kohno, T. Seki, S. D. Findaly, Y. Ikuhara, and N. Shibata, Nature (London) **602**, 234 (2022).

[55] M. Fiebig, D. Fröhlich, Th Lottermoser, and S. Kallenbach, Appl. Phys. Lett. **66**, 2906 (1995).

[56] J.-X. Qiu *et al.*, Nat. Mater. **22**, 583 (2023).